Physical Biology

OFFICIAL JOURNAL OF
Sociedad de Biofísicos Latino Americanos

ACCEPTED MANUSCRIPT

Using two dyes to observe the competition of Ca^{2+} trapping mechanisms and their effect on intracellular Ca^{2+} signals

To cite this article before publication: Estefania Piegari *et al* 2018 *Phys. Biol.* in press https://doi.org/10.1088/1478-3975/aac922

Using two dyes to observe the competition of Ca^{2+} trapping mechanisms and their effect on intracellular Ca^{2+} signals.

E. Piegari, L. F. Lopez and S. Ponce Dawson

Abstract

The specificity and universality of intracellular Ca^{2+} signals rely on the variety of spatio-temporal patterns that the Ca^{2+} concentration can display. Ca^{2+} liberation through inositol 1,4,5-trisphosphate receptors (IP_3Rs) is key for this variety. In this paper we study how the competition between buffers of different kinetics affects Ca^{2+} signals that involve Ca^{2+} release through IP_3Rs. The study also gives insight on the underlying spatial distribution of the channels that participate of the signals. Previous works on the effects of Ca^{2+} buffers drew conclusions "indirectly" by observing the Ca^{2+}-bound dye distributions in the presence of varying concentrations of exogenous buffers and using simulations to interpret the results. In this paper we *make visible the invisible* by observing the signals simultaneously with two dyes, Rhod-2 and Fluo-4, each of which plays the role of a slow or a fast Ca^{2+} buffer, respectively. Our observations obtained for different concentrations of Fluo-4 highlight the dual role that fast buffers exert on the dynamics, either reducing the intracluster channel coupling or preventing the channels inhibition and allowing the occurrence of relatively long cycles of Ca^{2+} release. Our experiments also show that signals with relatively high Ca^{2+} release rates remain localized in the presence of large Rhod-2 concentrations while the mean speed of the elicited waves increases. We interpret this as a consequence of the more effective uncoupling between IP_3R clusters as the slow dye concentration increases. Combining the analysis of the experiments with numerical simulations we also conclude that Ca^{2+} release not only occurs within the close vicinity of the centers of the clearly identifiable release sites (IP_3R clusters) but there are also functional IP_3Rs in between them.

Key words: Ca^2+ puffs, Ca^2+ buffers, kinetics, spatio-temporal distributions

1 Introduction

Calcium (Ca^{2+}) signaling is involved in many physiological processes [1, 2]. Ca^{2+} release from the endoplasmic reticulum (ER) through Inositol 1,4,5-trisphosphate receptors (IP_3Rs) is key: IP_3Rs are the primary cytosolic target for the initiation of intracellular Ca^{2+} signals [3]. IP_3Rs need to bind IP_3 and Ca^{2+} to become open [4]. Thus, they are affected by the so called *Calcium Induced Calcium Release* (CICR) [5]. IP_3R-mediated Ca^{2+} signals start with the release of Ca^{2+} through a single open IP_3R and eventually propagate by means of CICR. In most cells IP_3Rs are organized in clusters. The signals can then remain localized (*i.e.*, involving the release through one or more IP_3Rs in a cluster), or become global depending on the efficiency of the released Ca^{2+} to elicit the opening of IP_3Rs from many clusters [6–8]. Localized signals in which Ca^{2+} is released from the ER through IP_3Rs that belong to a single cluster are known as *puffs* [9]. Ca^{2+} puffs are the building blocks of more global signals such as waves. The end responses that are eventually elicited can be different depending on the amplitude and dynamics of intracellular Ca^{2+} [10–12] and on whether the Ca^{2+} signal remains localized (puffs) or propagates (waves) throughout the cell [13, 14]. Thus, there is information encoded in the spatio-temporal distribution of the intracellular Ca^{2+} concentration [15, 16]. Understanding the processes that modulate this distribution is key for the comprehension of the Ca^{2+} signaling toolkit.

Ca^{2+} signals can be reshaped through various mechanisms, among them, Ca^{2+} buffering [17, 18]. Cells contain different types of intracellular Ca^{2+} buffers to keep the free cytosolic Ca^{2+} concentration low since prolonged high elevations lead to cell death [1]. Buffers not only decrease the Ca^{2+} concentration but also change its spatio-temporal distribution [17, 18]. The resulting reshaping depends on buffer kinetics. Thus, cells could modify buffer concentrations to reshape Ca^{2+} signals and, in this way, change the responses that arise upon a given stimulus. The modification of IP_3R-mediated intracellular Ca^{2+} signals by buffers has been studied experimentally by observing the Ca^{2+} distribution that arises upon a controlled stimulus in the presence of various amounts of a slow (*e.g.*, EGTA) or fast (*e.g.*, BAPTA) buffer [17, 18]. In this way it was observed that EGTA speeds up Ca^{2+} signals, induces their spatial localization and can lead to signal amplitude potentiation. The addition of BAPTA, on the other hand, slows down the Ca^{2+} response and promotes signals that spread all over the cell [17]. In these experiments, the interaction of the added buffers with Ca^{2+} was observed indirectly using a single-wavelength Ca^{2+} dye that increases its fluorescence intensity upon Ca^{2+}-binding [19]. The fluorescent images of [17]

then reflected the Ca^{2+}-bound dye distribution which was the result of the combined effect of various competing processes, one of which was the binding of Ca^{2+} to the added exogenous buffer. Interpreting the observations was difficult not just because they depended on the competition between the various unobservable buffers and the dye for Ca^{2+} but also because different patterns of Ca^{2+} release could occur due to the effect of the exogenous buffer [20] or of the dye itself [21] on CICR. Having a good mathematical model of the Ca^{2+} dynamics with realistic biophysical parameters was then unavoidable not only to quantify the properties of the Ca^{2+} release that underlied the observations [22, 23] but also to interpret the effect that the added buffers had on the signals [24, 25].

In the present paper we take a somewhat different approach to study the role of buffers on IP_3R-mediated Ca^{2+} signals which provides more direct information. Namely, we observe the signals simultaneously with two Ca^{2+} dyes of different kinetics, Rhod-2 and Fluo-4, each of which plays the role of a slow or a fast Ca^{2+} buffer whose distribution is observed directly when bound to Ca^{2+}. Even if Fluo-4 is only slightly faster than Rhod-2, the analysis of the changes that are induced when the concentration of one of the two dyes is varied allows us to infer trends. Comparing the images obtained with different dye concentrations is not completely straightforward. In particular, it is difficult to infer whether the changes observed are due to differences in the Ca^{2+} release rate or only in the amount of Ca^{2+} that is bound to the observed dye. In order to overcome this problem we use numerical simulations to identify a quantity that increases with the underlying Ca^{2+} current regardless of the concentrations of dye used. Briefly, given a localized Ca^{2+} current, this quantity is the relative variation of the concentration of Ca^{2+} bound to one of the dyes that would have been obtained for that given current in the absence of the other dye. As explained later in the paper and in the Supplementary Material file, this quantity, which is meaningful in the case of localized release, can be estimated for each observed puff. In this way we can associate to each observed puff a value that is an increasing function of the underlying Ca^{2+} current. A comparison of the values we obtain for the various puffs observed in our experiments leads to the conclusion that the largest (peak) Ca^{2+} current that underlies observed puffs increases when the slow dye concentration increases and that the mean Ca^{2+} current decreases while the release duration increases when the concentration of the fast dye is increased. Applying the approach we introduced in [26], in this paper we derive, from the observed fluorescence, the distribution of Ca^{2+} bound to each of the dyes used. We then compare how the spatio-temporal dynamics of these distributions vary with the dye concentrations. In this way we are

able to observe directly that slow buffers cannot compete with the fast ones in the regions of fastest Ca^{2+} release and bind Ca^{2+} around those regions.

Given that Ca^{2+} signals are the result of various processes, varying Ca^{2+} buffering also allows the study of some of the other factors that shape the signals. In particular, the time and spatial range of IP_3R-mediated signals depends strongly on the ability of the released Ca^{2+} to elicit further Ca^{2+} release. The results we obtain for increasing amounts of the slow dye support the interpretation that the presence of slow buffers dirupts the Ca^{2+}-mediated coupling between IP_3R-clusters [21, 27]. Our experiments show, on the other hand, that the addition of the fast dye can decrease the localized Ca^{2+} current and allow the occurrence of long cycles of Ca^{2+} release. This result illustrates the dual role of fast buffers as moderators of the Ca^{2+}-mediated coupling between IP_3Rs in a cluster and as moderators of the channels inhibition. The last observation agrees with the results of the analytic study of [28] which showed that the addition of a fast Ca^{2+} buffer could decrease the mean interpuff time interval. The dual role that fast buffers can play has also been observed in numerical and modeling studies of the dynamics of isolated and clustered IP_3Rs [24, 25, 29]. Namely, these studies showed that the mean Ca^{2+} release duration increased in the case of clusters with closely packed IP_3Rs where the fast buffer was able to moderate the inhibiting effect of high Ca^{2+} concentrations on the channels. They showed, on the other hand, that the release duration decreased when the net effect of the buffer was to moderate Ca^{2+} coupling via CICR, an effect that took place in clusters where the mean inter-channel separation was large enough. These studies and others [30–32] also illustrate the relevance of the intra-cluter spatial organization on the emergent behavior of the cluster as a whole. Even if the channels are not directly observed in our experiments, our results give hints on their distribution. Using numerical simulations to interpret our experimental observations we conclude that Ca^{2+} is not only released from clusters that are 1.4-2 μm apart from one another, as could be inferred from the observation of puffs. Namely, our studies suggest the need of having "loose" functional IP_3Rs in between clusters to explain several of our observations, among them, the non-colocalization of the Ca^{2+}-bound Fluo-4 and Ca^{2+}-bound Rhod-2 maxima for low Rhod-2 concentrations and the disruption of the intercluster coupling by slow buffers.

2 Materials and Methods

2.1 Oocyte preparation

Experiments were performed on *Xenopus laevis* immature oocytes previously treated with collagenase. Oocytes were loaded by intracellular microinjection with different compounds. Two calcium dyes Fluo-4 dextran high affinity (K_d= 772 nM) and Rhod-2 dextran (K_d= 2000 nM) were used to probe cytosolic [Ca^{2+}]. Caged $InsP_3$ (D-Myo-Inositol 1,4,5-Triphosphate,P4(5)-(1-(2-Nitrophenyl)ethyl) Ester) was used to induce IP_3R opening. The exogenous Ca^{2+} buffer EGTA (Ethylene glycol-bis(2-aminoethylether)-N,N,N',N'-tetraacetic acid) was also used. Final intracellular concentrations of the different compounds were calculated assuming a 1 μl cytosolic volume. Final intracellular concentration of $InsP_3$ was 9 μM in all the experiments. Fluo-4, Rhod-2 and $InsP_3$ were from Molecular Probes Inc.; EGTA was from Sigma Aldrich. Recordings were made at room temperature.

2.2 Confocal microscopy

Confocal imaging was performed using a spectral confocal scanning microscope Olympus FluoView1000 that has a spectral scan unit connected to an inverted microscope IX81. The caged compound was photolyzed with the UV part of the spectrum of a mercury lamp that comes with the microscope using the modification introduced in [33]. Fluo-4 was excited with the 488 nm line of a multiline Argon laser, Rhod-2 was excited using the 543 nm line of a He-Ne laser. Both lasers were focused on the oocyte with a 60 $\times$ oil immersion objective (NA 1.35). The emitted fluorescence was detected in the 500-600 nm and the 600-630 nm ranges, respectively, with PMT detectors. All the experiments were performed in the linescan imaging mode to improve the temporal resolution. Linescan images were obtained by scanning along a fixed line (250 px) within the oocyte. The acquisition rate was fixed at 10 μs per pixel resulting in a scan rate of 3.26 ms per line. The caged compound was photo-released approximately 3 s after the linescan acquisition started. The UV uncaging pulse was $\sim$(100-200) ms long.

2.3 Image analysis

All images were analyzed using routines written in MATLAB [34]. In the experiments where we simultaneously acquired both fluorescence channels (around 510 nm for Fluo-4 and 570 nm for Rhod-2), we used a linear unmmixing method with coefficient 0.1626 to minimize the effect of the spectral

bleed-through as was done in [35]. The images were also smoothed by averaging over the 8 nearest pixels. This smoothing procedure gave the fluorescence, $f_D(x_i, t_j)$, at time t_j and point x_i of the linescan for each dye ($D = F$ for the wavelengths of emission of Fluo-4 and $D = R$ for those of Rhod-2).

2.3.1 Puff characterization

We show in Figs. 1(a) and (b) a typical linescan image with several puffs observed simultaneously with Fluo-4 and Rhod-2. We plot in these figures the fluorescence distribution, $f_D(x_i, t_j)$, as a function of space (vertical) and time (horizontal) for $D = F$ in (a) and $D = R$ in (b) using a color code as indicated in the accompanying bars. In order to identify Ca^{2+} puffs in the images we first determined, by visual inspection, regions that contained a localized connected set of pixels where the intensity was sufficiently above the basal level in the Fluo-4 and in the Rhod-2 channels (marked with arrows). Rectangular regions enclosing the connected sets were then extracted. An example of a rectangular region enclosing a puff that could be observed simultaneously in the Fluo-4 and Rhod-2 channels is shown in Figs. 1(c) (for Fluo-4) and (d) (for Rhod-2). For further processing we identified the position and time, (x_c, t_c), of the rectangular region with the largest fluorescence, f_D, as illustrated in Figs. 1(c)-(d). To compute the different puff parameters we worked with the ratios, $\Delta f_{r,D}$:

$$\Delta f_{r,D}(x_i, t_j) = \frac{f_D(x_i, t_j) - f_{0,D}(x_i)}{f_{0,D}(x_i)}. \quad (1)$$

where $f_{0,D}(x_i)$ is the fluorescence at spatial point, x_i, averaged over time before the photolysis flash (*i.e.*, for $t \leq t_{UV}$). To determine the amplitude and the temporal parameters of the puff located around the point, (x_c, t_c), of the image, we averaged $\Delta f_{r,D}$ over 11 horizontal lines (the line that corresponded to $x = x_c$, five below and five above it), as done in [21]. We show in Figs. 1(e) and (f) the time trace of the averages obtained, $\overline{\Delta f_{r,D}}$, for Fluo-4 and Rhod-2, respectively, in the case of the puff depicted in Figs. 1(c) and (d). We used these traces to compute the amplitude of the puffs, A_D (*i.e.*, the maximum over time of $\overline{\Delta f_{r,D}}$), and the rise, $t_{d,D}$, and decay, $t_{d,D}$, times for each dye, D, as done in [21] and illustrated in Figs. 1(e) and (f). We also computed the amplitude growth rate as $GR_D = 0.9 * \frac{A_D}{t_{r,D}}$.

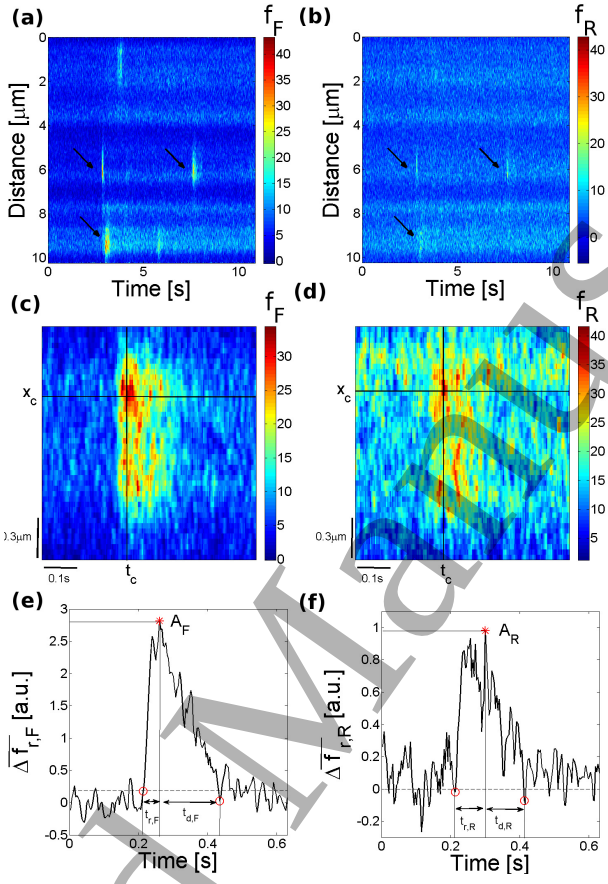

Figure 1: Puff characterization. (a), (b): Typical linescan image with several puffs (indicated with arrows) simultaneously observed with Fluo-4 (a) and Rhod-2 (b) in an experiment with $[F]_T = 36\ \mu M$, $[EGTA]_T = 45\ \mu M$ and $[R]_T = 90\ \mu M$. The color bar represents the fluorescence intensity f_D ($D = F$ for Fluo-4 and $D = R$ for Rhod-2). The horizontal and vertical axes correspond to time and space, respectively. (c), (d): Similar to (a), (b) but for a rectangular region containing one puff simultaneously observed with Fluo-4 (c) and Rhod-2 (d). The point, (x_c, t_c), corresponds to the location of the maximum of f_D over each shown image. (e), (f): Temporal profiles obtained from Figs. 1(c), (d), respectively, by averaging the corresponding $\Delta f_{r,D}$ ($D = F, R$) over eleven horizontal lines around x_c. The quantities with which we characterize the puff amplitude and time course are indicated in these figures.

2.3.2 Wave characterization

Waves were identified by visual inspection as events where Ca^{2+} release occurred at neighboring sites subsequently in time. Wave velocities for Fluo-4

were determined by selecting two points, (x_i, t_i), $i = 1, 2$, on the corresponding image as explained in what follows and then computing $V_F = |\frac{x_1 - x_2}{t_1 - t_2}|$. The points were chosen so that x_1 and x_2 corresponded to the space location of the neighboring sites and t_1 and t_2 were the times at which the fluorescence started to increase at each site (see Fig. 2(a)).

2.3.3 Ca^{2+}-bound dye distributions and mask images

We derived from the fluorescence distributions, f_D and $\Delta f_{r,D}$, the corresponding Ca^{2+}-bound dye and relative Ca^{2+}-bound dye concentrations, $[CaD]$ and $\Delta[CaD]_r \equiv ([CaD] - [CaD]_b)/[CaD]_b$, respectively, where D is the dye ($D = F$ for Fluo-4 and $D = R$ for Rhod-2) and $[CaD]_b$ is the basal Ca^{2+}-bound dye concentration. For this derivation we followed [26] neglecting fluctuations in the number of dye molecules that contribute to the fluorescence at each pixel (we assumed it was the same value, $\langle N_D \rangle$, for each dye concentration everywhere):

$$[CaD] = \frac{[D]_T}{q_{1,D} - q_{2,D}} \left(\frac{f_D}{\gamma_D \langle N_D \rangle} - q_{2,D} \right), \tag{2}$$

from which we obtained (see Supplementary Material):

$$\Delta[CaD]_r(x,t) = \Delta f_{r,D}(x,t) \left(1 + \frac{q_{2,D}}{q_{1,D} - q_{2.D}} \frac{[Ca]_b + K_{d,D}}{[Ca]_b} \right). \tag{3}$$

In Eqs. (2)–(3), $q_{2,D}$ and $q_{1,D}$ represent the (apparent) brightness of the free and the Ca^{2+}-bound dye molecules, respectively, γ_D is an amplification factor introduced by the detectors and $K_{d,D}$ is the dissociation constant, $K_{d,D} = k_{off-D}/k_{on-D}$, of the corresponding dye ($D = F, R$) – Ca^{2+} reaction. To compute the quantities in these equations we used numerical values of $q_{1,D}$, $q_{2,D}$, γ_D and $\langle N_D \rangle$ that we derived from the estimates of [26] ($q_{1,F} = 0.45$, $q_{2,F} = 0.01$, $\gamma_F = 5$ and $\langle N_F \rangle = 32$ for Fluo-4 and $q_{1,R} = 0.36$, $q_{2,R} = 0.02$, $\gamma_R = 6$ and $\langle N_R \rangle = 32, 80$ for $[R]_T = 36$ and 90 μM, respectively) and used $[\mathrm{Ca}]_b = 100\ nM$. More details may be found in the Supplementary Material.

We also generated mask images of the Ca^{2+}-bound dye distributions using a 0.6 CaD_{max} threshold where CaD_{max} is the maximum of $[CaD]$ over the whole image. We illustrate in Fig. 2 the processing performed with an image observed in the Fluo-4 channel. From the fluorescence, f_F (Fig. 2(a)), observed as a function of space and time we derived the corresponding $[CaF]$ ((Fig. 2(b))) using Eq. (2) for $D = F$. We then computed the maximum, CaF_{max}, over the image in Fig. 2(b) and generated the mask (Fig. 2(c)) using 0.6 CaF_{max} as the threshold.

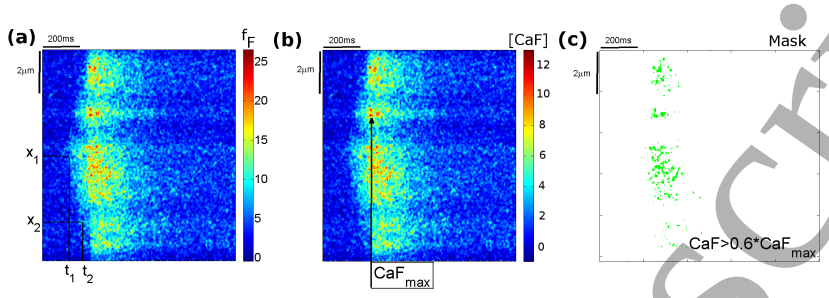

Figure 2: Typical wave observed with Fluo-4 in an experiment with $[F]_T = 36\ \mu M$, $[EGTA]_T = 45\ \mu M$ and $[R]_T = 90\ \mu M$. The horizontal and vertical axes correspond to time and space, respectively. (a): The velocity of the wave in the Fluo-4 channel is determined by selecting two points, (x_i, t_i), $i = 1, 2$, on the image as explained in the main text and then computing $V_F = \mid \frac{x_1 - x_2}{t_1 - t_2} \mid$. The color bar represents the fluorescence intensity f_F. (b) $[CaF]$ distribution obtained from (a) using Eq. (2) for $D = F$. (c) Mask image computed from (b) using a 0.6 CaF_{max} threshold with CaF_{max} the maximum value of $[CaF]$ in (b).

2.4 Numerically simulated reaction-diffusion model

We performed numerical simulations of the cytosolic Ca^{2+} dynamics solving a set of reaction-diffusion equations in a spherical volume (assuming spherical symmetry with r the radial coordinate) for: Ca^{2+}, an immobile endogenous buffer (S), two cytosolic indicators (F and R) and an exogenous mobile buffer (EGTA). A point source located at the origin and pumps (P) that removed Ca^{2+} uniformly in space were also included. The Ca^{2+} sources that we are dealing with in the experiments are IP_3R clusters. Our simulations do not resolve the intra-cluster dynamics as done in [20, 28, 30, 32]. The aim of our simulations is to describe, as simply as possible, how the Ca^{2+} bound-dye distribution varies with the dye concentrations around a localized Ca^{2+} source which is simply represented by a point. For the source we assumed that it consisted of n_c channels that opened simultaneously at $t = 0$ s each of which released a constant current, $I_{Ca} = 0.1\ pA$. We assumed that the channels closed after a random time that was drawn from an exponential distribution with mean, $t_{open} = 20\ ms$ [36]. For the Ca^{2+}-buffer or dye reactions we considered that a single Ca^{2+} ion bound to a single buffer or dye molecule (X) according to:

$$Ca^{2+} + X \underset{k_{on-X}}{\overset{k_{off-X}}{\rightleftarrows}} CaX. \tag{4}$$

In Eq. (4), X represents F, R, EGTA, or S and k_{on-X} and k_{off-X} are the forward and backward binding rate constants of the corresponding reaction, respectively. We assumed that each species, X, diffused with the same coefficient, D_X, in its free and Ca^{2+}-bound forms and that their total concentration, $[X]_T$, was spatially uniform at $t = 0$. Thus, $[F]_T$, $[R]_T$, $[EGTA]_T$, and $[S]_T$, remained uniform and constant for all times and we calculated the free concentrations, $[F]$, $[R]$, $[EGTA]$, and $[S]$, by subtracting the concentration of their Ca^{2+} bound forms to their total concentrations. The dynamical equations of the model were then given by:

$$\begin{aligned} \frac{\partial [Ca^{2+}]}{\partial t} &= D_{Ca}\nabla^2[Ca^{2+}] - \sum_{X=F,R,S,EGTA} R_{CaX} \\ &\quad +\sigma\ \delta(\mathbf{r}) - v_p \frac{[Ca^{2+}]^2}{[Ca^{2+}]^2 + k_p^2}, \end{aligned} \tag{5}$$

$$\frac{\partial [CaX]}{\partial t} = D_X\nabla^2[CaX] + R_{CaX}; \quad X = F, R, S, EGTA \tag{6}$$

with $\sigma = 20758 \cdot N_o(t) \cdot I_{Ca}\ \mu M \mu m^3/s$; $N_o(t)$, the number of simultaneously open channels at time, t; D_{Ca}, the free diffusion coefficient of Ca^{2+} and the reaction terms:

$$R_{CaX} = k_{on-X}[Ca^{2+}]([X]_T - [CaX]) - k_{off-X}[CaX]. \tag{7}$$

The reaction-diffusion of Eqs. 5 and 6 were solved with no flux boundary conditions at $r = 20.5\ \mu m$ using a backward Euler method in time and an explicit finite-difference formula in space with a 2nd order expression (first neighbors) for the Laplacian. The spatial grid size was $dr = 0.041$ μm and the time step $dt = 10\ \mu s$. For the initial condition, we assumed that all concentrations were in equilibrium with Ca^{2+} at its (uniform) basal concentration, $[Ca]_b$. The values of the parameters used in the simulations (taken from [21]) are listed in Table 1.

To compare the results with the experimental confocal images we calculated a weighted average of $[CaD]$ for each dye ($D = F, R$) along the line-scan $r = (x, 0, 0)$ according to the confocal microscope point spread function (PSF):

$$\overline{[CaD]}(x,t) = \frac{1}{V}\int [CaD](r',t')\ \exp\left(-2\left(\frac{(x-x')^2 + y'^2}{w_r^2} + \frac{z'^2}{w_z^2}\right)\right) dx'dy'dz', \tag{8}$$

where $w_r = 0.23\ \mu m$, $w_z = 1.15\ \mu m$ and $V = w_r^2 w_z \frac{\pi}{2}^{3/2}$. This is the blurred version of the Ca^{2+}-bound dye concentration ($\overline{[CaD]}$). We show in Fig. 3 an

Parameter	Value	Units
Free Calcium		
D_{Ca}	220	μm^2 s^{-1}
$[Ca]_b$	0.05-0.1	μM
Calcium dye Fluo-4-dextran		
D_F	15	μm^2 s^{-1}
k_{on-F}	240	$\mu M^{-1} s^{-1}$
k_{off-F}	180	s^{-1}
$[F]_T$	0, 36	μM
Calcium dye Rhod-2-dextran		
D_R	15	μm^2 s^{-1}
k_{on-R}	70	$\mu M^{-1} s^{-1}$
k_{off-R}	130	s^{-1}
$[R]_T$	0, 36, 90	μM
Exogenous buffer EGTA		
D_{EGTA}	80	μm^2 s^{-1}
$k_{on-EGTA}$	5	$\mu M^{-1} s^{-1}$
$k_{off-EGTA}$	0,75	s^{-1}
$[D]_T$	45, 90	μM
Endogenous immobile buffer		
D_S	0	μm^2 s^{-1}
k_{on-S}	400	$\mu M^{-1} s^{-1}$
k_{off-S}	800	s^{-1}
$[S]_T$	300	μM
Pump		
k_p	0.1	s^{-1}
v_p	0.9	$\mu M\ s^{-1}$
Source		
n_c	3, 6, 10, 15, 30	-
t_{open}	20	ms
I_{Ca}	0.1	pA

Table 1: Parameter values used to solve the simulations.

example of a numerical simulation performed using the parameters of Table 1 with $[F]_T = 36\ \mu M$, $[EGTA]_T = 45\ \mu M$ and $[R]_T = 90\ \mu M$ and with a source of $n_c = 10$ channels that opened simultaneously at $t = 0$, each of which released a constant current, $I_{Ca} = 0.1\ pA$, and closed after a random time that was drawn from an exponential distribution of mean, $t_{open} = 20$

ms. We plot in Fig. 3(a) the Ca^{2+} current, $I(t)$, used in the simulation and in Figs. 3(b) and (c) the obtained blurred distributions of Ca^{2+}-bound to Fluo-4, $\overline{[CaF]}$, and to Rhod-2, $\overline{[CaR]}$, respectively. In order to compute the equivalent of $\Delta f_{r,D}$ (Eq. (1)) for the simulations we calculated the relative increment in $\overline{CaD}$ as:

$$\Delta[CaD]_r = \frac{\overline{[CaD]} - \overline{[CaD]}_b}{\overline{[CaD]}_b} \equiv \frac{\Delta[CaD]}{\overline{[CaD]}_b}, \tag{9}$$

with $\overline{CaD}_b$ as in Eq. (8) for the Ca^{2+}-bound dye concentration at basal conditions.

We also relied on the numerical simulations to asses the rate of CICR-mediated coupling between neighboring clusters. To this end we used the concentration, $[Ca^{2+}](d,\tau)$, obtained numerically at distance $|\mathbf{r}| = d$ from the Ca^{2+} source and time, τ, after the initiation of the release to calculate the probability, $P_0(d,t)$, that an IP_3R within a cluster with n_s IP_3-bound IP_3Rs located at a distance, d, from the source becomes open by time, t. We computed:

$$P_0(d,t) = 1 - \exp\left(-\int_0^t d\tau\, n_s k_{on}[Ca^{2+}](d,\tau)\right) \tag{10}$$

with $k_{on} = 20\ \mu M^{-1}s^{-1}$ the rate of Ca^{2+} binding to the IP_3R activating site of the DeYoung-Keizer model [36]. We illustrate this computation in Figs. 3(d) and (e). We show in Fig. 3(d) three snapshots of the free Ca^{2+} distribution as a function of the distance to the source for the same simulation as in Figs. 3(a)–(c). We indicate in this figure the "sensing" distance, d. We plot in Fig. 3(e) the free Ca^{2+} concentration at this distance as a function of time, τ. Integrating this concentration up to a given time, t, as indicated in the figure, we compute the open probability, $P_0(d,t)$, given by Eq. (10).

2.5 Comparison of Ca^{2+} release amplitudes between experiments performed under different conditions.

The comparison of Ca^{2+} images obtained from experiments performed under different conditions is not completely straightforward since the changes observed could be due to differences in the Ca^{2+} release rate or in the amount of Ca^{2+} that is bound to the dye. Numerical studies can provide a hint on how images of the same Ca^{2+} release event change when observed under varying concentrations of the dyes. This is what we analyzed in the Supplementary Material. Here we explain how we processed the experimental images to obtain a quantity that, according to the simulations, increases with the Ca^{2+}

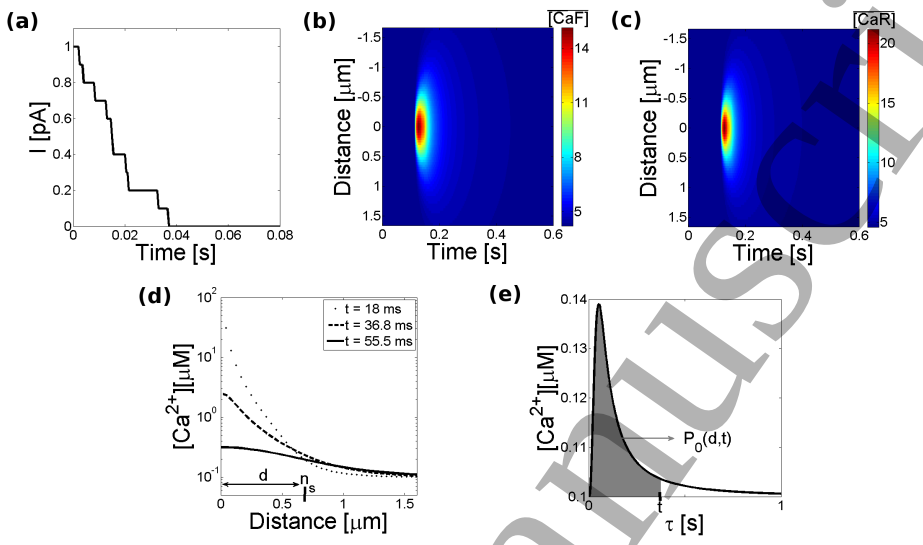

Figure 3: Example of a numerical simulation performed as described in the text. (a) Ca^{2+} current, I, as a function of time, t. In this case 10 channels are simultaneously open at $t = 0$ and then close randomly after a mean time, $t_o = 20\ ms$. (b) Simulated blurred Ca^{2+}-bound Fluo-4 distribution. (c) Similar to (b) but for the Ca^{2+}-bound Rhod-2 distribution. In (b) and (c), the horizontal and vertical axes correspond to time and space, respectively. The color code represents concentrations in μM as shown with the color bars. Inserting these blurred concentrations in Eq. (9) we compute the relative increments, $\Delta[CaD]_r$, for $D = F$ and $D = R$. (d) $[Ca^{2+}]$ as a function of the distance to the source at three different times. (e) $[Ca^{2+}]$ at the distance, d, indicated in (d), where we assume there are n_s sensing channels. Integrating $[Ca^{2+}](d, \tau)$ up to $\tau = t$ (shaded area) we compute the probability, $P_0(d, t)$, that one of the n_s channels opens by time, t, as prescribed by Eq. (10).

release rate regardless of the two dye concentrations used in each experiment. We first computed $\Delta[CaF]_r$ and $\Delta[CaR]_r$ for each Ca^{2+}-release event observed experimentally as explained in Sec. 2.3.3. We then computed their maximum values over the observed region, $\Delta[CaF]_{r,M}$ and $\Delta[CaR]_{r,M}$. We subsequently used the total Rhod-2 concentration, $[R]_T$, of the corresponding experiment to obtain an estimate of the maximum value of $\Delta[CaF]_r$ that would have been attained for the same release event if only Fluo-4 had been present. We repeated the procedure using $[F]_T$ to estimate the maximum value of $\Delta[CaR]_r$ that would have been attained if only Rhod-2 had been present. As shown in the Supplementary Material file, these estimates that we call, respectively, A_{lib-F} and A_{lib-R}, are increasing functions of the underlying Ca^{2+} current independently of the total dye concentrations that are

used if the current arises in a very localized region. The results of the simulations presented in the Supplementary Material file further show that, for a given (localized) Ca^{2+} current, the difference $A_{lib-F} - \Delta[CaF]_{r,M}$ is linearly proportional to the concentration, $[R]_T$, used in the simulations and that the constant of proportionality is weakly dependent on the current. Analogously, $A_{lib-R} - \Delta[CaR]_{r,M}$ is linearly proportional to $[F]_T$. Based on these results, in the experiments we estimate A_{lib-F} and A_{lib-R} from $\Delta[CaF]_{r,M}$ and $\Delta[CaR]_{r,M}$, respectively, as:

$$\begin{aligned} A_{lib-F} &\approx \Delta[CaF]_{r,M} + \alpha_{F,R}[R]_T, \\ A_{lib-R} &\approx \Delta[CaR]_{r,M} + \alpha_{R,F}[F]_T \end{aligned} \tag{11}$$

with $\alpha_{F,R} = 4.58 \cdot 10^{-3}\ \mu M^{-1}$ and $\alpha_{R,F} = 1.16 \cdot 10^{-3}\ \mu M^{-1}$.

To have quantities that reflect more directly the underlying Ca^{2+} current and the total Ca^{2+} released during the event we computed, respectively, the growth rate, $GR\text{-}A_{lib-D} = 0.9 * \frac{A_{lib-D}}{t_{r,D}}$ and $I_{lib-D} = A_{lib-D} \cdot t_{r,D}$ for each dye ($D = F$ for Fluo-4 and $D = R$ for Rhod-2). A_{lib-D}, $GR\text{-}A_{lib-D}$ and I_{lib-D} are reporters of the maximum Ca^{2+} concentration, of the Ca^{2+} current and of the total amount of Ca^{2+} released during the time course of the event, respectively.

3 Results

We show in this Section some of the results of the Ca^{2+} imaging experiments peformed as described in Materials and Methods. The different concentrations of dyes and EGTA used in each experiment are detailed in Table 2 where we classify the experiments in 6 sets. In particular we focus on how the signals change with the concentrations of the dyes, $[F]_T$ and $[R]_T$, as a way to understand how fast (in this case, Fluo-4) or slow (in this case, Rhod-2) buffers affect the spatio-temporal dynamics of cytosolic Ca^{2+}. To this end we first validate the assumption that Rhod-2 acts as a slow buffer and Fluo-4 as a fast one by looking at how the distributions of the puff properties observed in the Fluo-4 or the Rhod-2 fluorescence channel change, respectively, with $[R]_T$ or $[F]_T$. This analysis is contained in the Supplementary Material file. As shown in this file, the mean rise time of the puffs decreases and their growth rate increases with increasing $[R]_T$ which is consistent with previous results obtained for increasing slow buffer concentration [17, 18]. Although the results obtained with varying $[F]_T$ are not conclusive, the fraction of small amplitude and large rise time puffs observed with Rhod-2 increased with increasing Fluo-4 while their mean amplitude decreased. This agrees

with previous observations [17, 18] that show a more continuous Ca^{2+} release, albeit of smaller amplitude, when adding a fast buffer. We then analyze whether the changes correspond solely to variations in the observed fluorescence or if the underlying Ca^{2+} current is also modified when the dye concentrations are varied. We describe in what follows the results obtained when doing this and when analyzing the spatio-temporal distribution of $[CaF]$ and $[CaR]$. We end the Section showing the results of numerical simulations that suggest the need of having functional IP_3Rs between IP_3R-clusters to explain the observations.

Experiment	$[F]_T$ (μM)	$[R]_T$ (μM)	$[EGTA]_T$ (μM)
Set **I**	36	90	90
Set **II**	36	36	90
Set **III**	36	0	90
Set **IV**	36	90	45
Set **V**	36	36	45
Set **VI**	0	90	45

Table 2: Combinations of the dyes and EGTA concentrations used in the different experiments. We classify the experiments in 6 sets.

3.1 Changes in Ca^{2+} release with varying buffer concentrations observed in the experiments.

In order to determine whether the underlying Ca^{2+} current changes when the dye concentrations are varied we compute the quantities, A_{lib-D}, with $D = F$ for Fluo-4 or $D = R$ for Rhod-2, as described in Sec. 2.5. We show in Figs. 4(a) and (b) the CDFs of A_{lib-F} (*i.e.*, A_{lib} computed from the fluorescence observed in the Fluo-4 channel) and of its growth rate, $GR\text{-}A_{lib-F}$, for experiments with $[F]_T = 36\ \mu M$, $[EGTA]_T = 45\ \mu M$ and $[R]_T = 36\ \mu M$ (*i.e.*, Set **V** of Table 2, with dotted line) or $[R]_T = 90\ \mu M$ (*i.e.*, set Set **IV**, with solid line). The mean values of A_{lib-F} and $GR\text{-}A_{lib-F}$ increase as $[R]_T$ is increased ($\langle A_{lib-F}\rangle = 2.6$, $\langle GR\text{-}A_{lib-F}\rangle = 38\ s^{-1}$ for Set **V** and $\langle A_{lib-F}\rangle = 3.1$, $\langle GR\text{-}A_{lib-F}\rangle = 60\ s^{-1}$ for Set **IV**). As discussed later, the differences obtained indicate that the largest Ca^{2+} current that underlies the observed puffs increases as the concentration of the slow dye, Rhod-2, is increased. The change in the A_{lib-F} and $GR\text{-}A_{lib-F}$ distributions illustrated in Figs. 4(a)–(b) is accompanied by a change in the mean velocity of the waves observed in the same two experiment types as shown in Fig. 4(c) where we have plotted the CDFs of the velocity of the waves observed in the Fluo-4 channel (see V_F in Sec. 2.3.2) in experiments with $[F]_T = 36\ \mu M$,

$[EGTA]_T = 45\ \mu M$ and $[R]_T = 36\ \mu M$ (*i.e.*, Set **V** of Table 2, with dotted line) or $[R]_T = 90\ \mu M$ (*i.e.*, set Set **IV**, with solid line). The mean velocity gets bigger when $[R]_T$ is increased (from $\langle V_F \rangle = 22\ \mu m/s$ to $\langle V_F \rangle = 27\ \mu m/s$ for $[R]_T = 36$ and $90\ \mu M$, respectively). As discussed later in more detail, the changes analyzed so far can be interpreted within a unified framework by assuming that larger values of $[R]_T$ disrupt the CICR mediated inter-cluster coupling more efficiently.

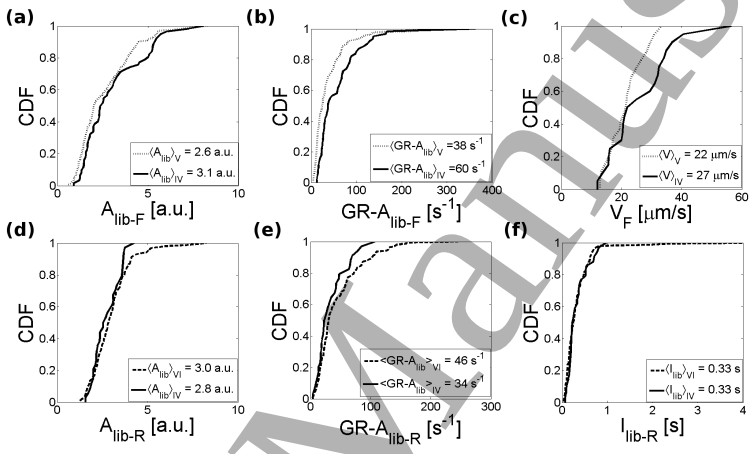

Figure 4: Estimation of Ca^{2+} release properties. (a) CDFs of A_{lib-F} (A_{lib} computed from the fluorescence observed in the Fluo-4 channel) for experiments performed with $[F]_T = 36\ \mu M$ and $[EGTA]_T = 45\ \mu M$ when Rhod-2 concentration is varied from $[R]_T = 90\ \mu M$ (Set **IV** of Table 2) to $36\ \mu M$ (Set **V**). The solid line corresponds to Set **IV** and the dotted line to Set **V**. (b) Similar to (a) but for the growth rate of A_{lib-F} distributions. (c) Similar to (a) but for the wave velocity distributions observed with Fluo-4. (d) CDFs of A_{lib-R} (A_{lib} computed from the fluorescence observed in the Rhod-2 channel) for experiments performed with $[R]_T = 90\ \mu M$ and $[EGTA]_T = 45\ \mu M$ when Fluo-4 is added. The solid line corresponds to Set **IV** of Table 1 and the dashed line to Set **VI**. (e) Similar to (d) but for the growth rate of A_{lib-R} distributions. (f) Similar to (d) but for I_{lib-R}.

In Figs. 4(d) and (e) we present the CDFs of A_{lib-R} (*i.e.*, A_{lib} computed from the fluorescence observed in the Rhod-2 channel) and the growth rate of A_{lib-R}, respectively, for experiments with $[R]_T = 36\ \mu M$, $[EGTA]_T = 45\ \mu M$ and $[F]_T = 0\ \mu M$ (*i.e.*, Set **VI** of Table 2, dashed line) and $[F]_T = 36\ \mu M$ (*i.e.*, Set **IV**, solid line). In this case $\langle A_{lib-R} \rangle$ decreases when Fluo-4 is added (from 3.0 for Set **VI** to 2.8 for Set **IV**) and events with the largest A_{lib-R} observed in Set **VI** are not observed in Set **IV**. The distribution of $GR\text{-}A_{lib-R}$, the quantity that is more directly linked to the underlying cur-

rent presents a similar behavior. The fraction of puffs with the largest rise times observed with Rhod-2, on the other hand, increases with increasing $[F]_T$ (see Supplementary Material). The changes observed in the distributions of A_{lib-R}, $GR\text{-}A_{lib-R}$ and rise time seem to indicate that there is a more continuous release at a slower rate when the fast dye concentration, $[F]_T$, is increased. This conclusion is consistent with the fact that the distribution of I_{lib-R} shown in Fig. 4(f) and the mean value, $\langle I_{lib-R} \rangle$, remain almost unchanged with increasing $[F]_T$.

3.2 Differences in the spatial distributions of CaF and CaR in experimentally observed puffs.

We now analyze the spatial distributions of CaF and CaR focusing on the points where their concentrations are maximal. To this end we first compute the Ca^{2+}-bound dye distributions for each image as explained in Materials and Methods. We then compute, for each puff that could be observed simultaneously with both dyes, the distance, δ, between the location of the maximum (in space and time) of CaF and the maximum of CaR. We show in Fig. 5 the distributions of the values of δ obtained in the experiments performed with $[F]_T = 36\,\mu M$ (Set **V**, Set **IV**, Set **II** and Set **I** of Table 2). Figs. 5(a) and (b) correspond to $[EGTA]_T = 45\ \mu M$ and Figs. 5(c) and (d) to $[EGTA]_T = 90\ \mu M$. $[R]_T$ increases from 36 to 90 μM when going from (a) to (b) or from (c) to (d). We observe that for both $[EGTA]_T = 45\ \mu M$ and 90 μM the distributions of δ are concentrated around smaller values as $[R]_T$ is increased. This means that, for $[R]_T = 36\ \mu M$, Rhod-2 is not able to follow the dynamics of the signal near the source, while for larger $[R]_T$ (90 μM) Rhod-2 competes more efficiently with Fluo-4 for Ca^{2+} so that both maxima tend to co-localize. This different spatial distribution of Ca^{2+}-bound Rhod-2 and Fluo-4 is also reflected in Fig. 6 where we show mask images obtained as described in Materials and Methods for the case of four examples. There we observe that, for $[R]_T = 36\ \mu M$, $[CaR]$ attains its largest values (shown in red) in regions that surround those where $[CaF]$ is largest (shown in green). For $[R]_T = 90\ \mu M$, the region with largest $[CaR]$ overlaps with that of $[CaF]$ (yellow pixels) extending further around it in the case of small $[EGTA]_T$ (see red pixels in the surroundings of the green/yellow region in Fig. 6(b) which are absent in Fig. 6(d)). This analysis not only has implications for how the two dyes compete for Ca^{2+} (see Discussion) but also leads to the conclusion that the correction that is implicit in the computation of A_{lib-F} may be unnecessary for the experiments with $[R]_T = 36\ \mu M$. Namely, the assumption that A_{lib-F} or A_{lib-R} are increas-

ing functions of the Ca^{2+} release rate derives from simulations with a Ca^{2+} point source. If the maxima of $[CaR]$ and $[CaF]$ approximately co-localize, then the competition of Rhod-2 and Fluo-4 for the same Ca^{2+} occurs similarly to the case of a point source. Therefore, we expect the computation of A_{lib} to still provide an increasing function of the underlying Ca^{2+} current. If the maxima do not co-localize, however, the correction may not be necessary. Recomputing A_{lib-F} with $\alpha_{F,R} = 0\ \mu M^{-1}$ for the experiments with $[R]_T = 36\ \mu M$ we obtain CDFs that are slightly shifted to the left with respect to those of Fig. 4(a) or the equivalent one for $[EGTA]_T = 90\ \mu M$, but the basic trends remain unchanged (data not shown). Based on this we still conclude that there are (more) events with larger Ca^{2+} currents that remain spatially localized as $[R]_T$ is increased.

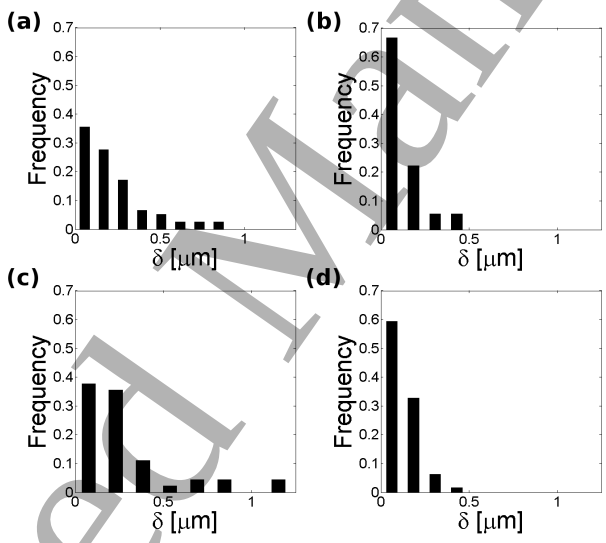

Figure 5: Distributions of the distance, δ, between the locations of the maxima (in space and time) of $[CaF]$ and $[CaR]$ for the Ca^{2+} puffs observed in experiments performed with the concentrations of Sets **V**, **IV**, **II** and **I** (see Table 2) in (a), (b), (c) and (d), respectively. With more detail, experiments were performed with $[F]_T = 36\ \mu M$. (a) and (b) correspond to $[EGTA]_T = 45\ \mu M$ and (c) and (d) to $[EGTA]_T = 90\ \mu M$. $[R]_T$ increases from 36 to 90 μM when going from (a) to (b) or from (c) to (d).

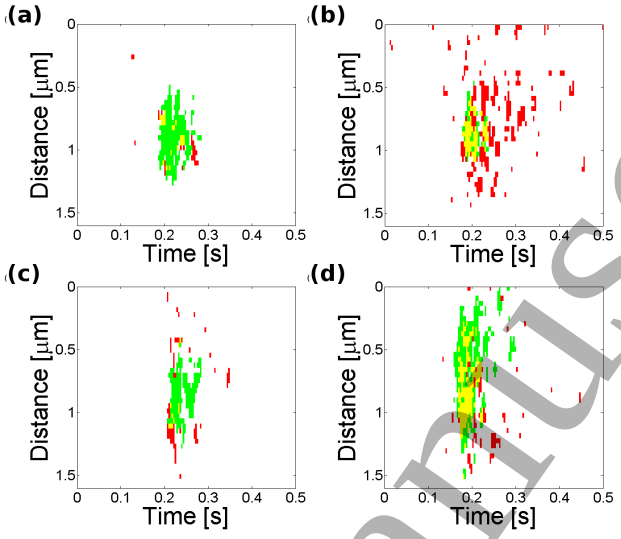

Figure 6: Typical puff mask images. The pixels where $[CaD] \geq 0.6\, CaD_{max}$ are shown in green for $D = F$ and in red for $D = R$. Yellow pixels are those in which the two masks co-localize. (a) and (c) correspond to $[R]_T = 36\ \mu M$ (Set **V** and Set **II** of Table 2, respectively) and (b) and (d) to $[R]_T = 90\ \mu M$ (Set **IV** and Set **I**, respectively).

3.3 Differences in the spatial distributions of CaF and CaR in experimental events involving multiple release sites.

We now analyze the competition between Rhod-2 and Fluo-4 for Ca^{2+} comparing the spatio-temporal distributions of CaR and CaF in experimentally observed events that involve Ca^{2+} release from multiple sites. As in the previous Section, CaR and CaF were derived from the observed fluorescence as explained in Sec. 2.3.3. We show in Fig. 7 two examples observed in experiments with $[F]_T = 36\ \mu M$, $[R]_T = 90\ \mu M$ and $[EGTA]_T = 45\ \mu M$ (Set **IV** of Table 2). The Ca^{2+}-bound Fluo-4 and the Ca^{2+}-bound Rhod-2 distributions are shown, respectively, in Figs. 7(a) and (b) for the first example and in Fig. 7(c) and (d) for the second one. Spatial averages of $[CaF]$ (gray) and $[CaR]$ (black) over the regions 1 and 2 defined in Fig. 7(a) are shown in Figs. 7(e) and (f) and the corresponding averages over the regions 1 and 4 defined in Fig. 7(c) are shown in Figs. 7(g) and (h). The bar to the right of Fig. 7(d) displays the spatial locations of the pixels at which, at some instant during the time course spanned by the images in Figs. 7(c) and (d), $[CaF]$ (green) or $[CaR]$ (red) are higher than 60% of CaF_{max} and CaR_{max}, respectively, with yellow indicating the pixels that meet both the conditions

for $[CaF]$ and $[CaR]$. In the first example, $[CaR]$ is initially larger in region 2 than in region 1. This results in a much slower increase of $[CaF]$ in region 2 which is also delayed with respect to the increase in $[CaF]$ in region 3. Rhod-2 is capturing Ca^{2+} more efficiently in region 2 than in others slowing down (though not preventing) the rise in $[CaF]$. This larger $[CaR]$ in region 2 does not translate, however, into a faster increase of $[CaR]$ with respect to that of $[CaF]$.

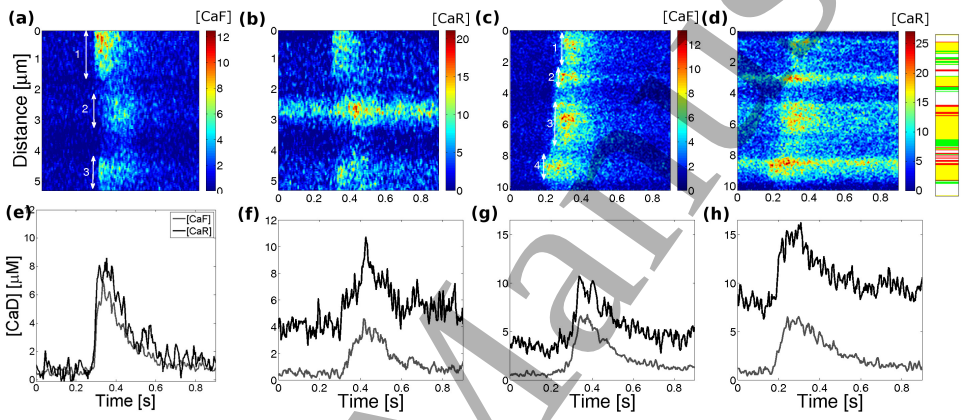

Figure 7: Dynamics of Ca^{2+}-bound Fluo-4 and Ca^{2+}-bound Rhod-2 in events that involve Ca^{2+} release from multiple sites. (a), (b), (e) and (f) correspond to one example, (c), (d), (g) and (h) to the other. They both were observed during Set **IV** experiments. (a), (c): $[CaF]$. (b), (d): $[CaR]$. (e), (f): Averaged profiles of $[CaF]$ (gray) and $[CaR]$ (black) computed over the regions 1 (e) and 2 (f) defined in (a) and over the regions 1 (g) and 4 (h) defined in (c). The color bars represent levels of $[CaF]$ and $[CaR]$ in μM. The bar to the right of (d) corresponds to the location of the pixels that, at any given time during the time-course of the images in (c)-(d), $[CaF]$ (green) or $[CaR]$ (red), exceed 60% of their corresponding maxima.

Comparing the "coupling" between the regions 4 and 3 and 3 and 2 of the second example we observe in Fig. 7(c) that the time elapsed between the beginning of the CaF fluorescence increment in regions 4 and 3 is larger than the time that separates the beginnings of the equivalent increments in regions 3 and 2. This delay of the coupling between regions 3 and 4 compared to that of regions 2 and 3 correlates with larger $[CaR]$ values in region 4 than in other regions. Furthermore these larger values are spread over most of region 4 especially over its upper part as illustrated by the bar to the right of Fig. 7(d). The presence of larger amounts of Rhod-2 in region 1 then seems to be hindering the coupling between the release sites located in this region and those in neighboring ones. The different behaviors observed in

$[CaF]$ depending on $[R]_T$ are further illustrated in Figs. 7(g) and (h) where we show the values of $[CaF]$ (gray) and $[CaR]$ (black) averaged over regions 1 and 4, respectively. As observed in Fig. 7(f), also in this example Fluo-4 binds Ca^{2+} more slowly where $[CaR]$ is higher.

3.4 Numerical Simulations: the need of having functional IP_3Rs between clusters to explain the observations

We here use numerical simulations to interpret how the changes in the relative location of the maxima in $[CaR]$ and $[CaF]$ obtained in the experiments and shown in Figs. 5 and 6 could be produced when varying $[R_T]$. To this end we simulate the reaction-diffusion model described in Sec. 2.4 using always the same (point) Ca^{2+} source (with $n_c = 10$) and basal Ca^{2+} ($[Ca]_b$=0.1 μM). We then generate mask images of the Ca^{2+}-bound dye, D, distributions ($D = F$ for Fluo-4 and $D = R$ for Rhod-2) obtained in the simulations using the same criterion that we applied to the experimental images. Namely, we used a 0.6 CaD_{max} threshold with CaD_{max} the maximum value of $[CaD]$ over the whole numerically simulated image (*i.e.* maximum value in space and time). We show two examples in Fig. 8, the one for Set **V** (Sets described in Table 2) in Fig. 8(a) and the one for Set **IV** in Fig. 8(b). The only difference between these two simulations is the value, $[R]_T$, which is 36 μM in (a) and 90 μM in (b). In both figures the mask derived from $[CaF]$ is shown in green, the one derived from $[CaR]$ in red and the overlapping region in yellow. We observe in the figures that the two masks overlap almost everywhere. In particular, the local (and global) maxima of both $[CaF]$ and $[CaR]$ occur at the location of the Ca^{2+}-point source. We also observe that, differently from what we find in the experiments, $[CaF]$ is spread over a (slightly) wider region than $[CaR]$. Both the overlapping and the $[CaF]$ dominated regions seem to be a little wider (both in space and time) in (a) than in (b), but their difference is minuscule. Similar regions were obtained in the simulations for Set **II** and Set **I**. If we increase the underlying Ca^{2+} current we obtain qualitatively similar images as well. We thus conclude that the mask images do not display noticeable differences when the concentrations of dye and EGTA are varied as in the experiments if the underlying Ca^{2+} current remains localized.

The comparison of Figs. 6 and 8 puts into question that functional IP_3Rs are limited to clusters that are $\sim 1.4\ \mu m$ apart. We now look further into this problem by analyzing the changes in Ca^{2+} release with $[R_T]$ that we inferred from Figs. 4 (a)-(c) and the equivalent ones obtained for the experiments with $[EGTA] = 90\ \mu M$. Based on these results we concluded that the

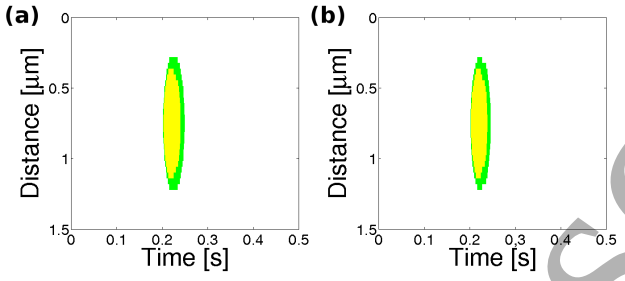

Figure 8: Numerical simulated mask images. The pixels where $\overline{[CaD]} \geq 0.6\, CaD_{max}$ are shown in green for $D = F$ and in red for $D = R$. Yellow pixels are those in which the two masks co-localize. (a) corresponds to $[R]_T = 36\ \mu M$ (Set **V** of Table 2) and (b) to $[R]_T = 90\ \mu M$ (Set **IV**).

presence of larger amounts of a slow buffer allowed the occurrence of puffs with larger underlying Ca^{2+} currents. As discussed in [21], this counter-intuitive result can, in principle, be explained in terms of a more efficient uncoupling between IP_3R clusters due to the presence of the slow buffer. We here use numerical simulations to determine whether increasing $[R_T]$ as in the experiments of Figs. 4 (a)-(b) can disrupt the CICR mediated coupling between IP_3R clusters that are $\sim 1.4\ \mu m$ apart. To this end we perform numerical simulations as before with a point Ca^{2+} source with n_c open IP_3Rs at $t = 0$. We then compute the probability, $P_0(d, t)$, that a channel within an IP_3R cluster with n_s IP_3-bound IP_3Rs located at a distance, d, from the original source becomes open by time t (see Materials and Methods). We show in Fig. 9(a)-(c) the open probability, $P_0(d, t)$ for experiments with $[F]_T = 36\ \mu M$, $[EGTA]_T = 45\ \mu M$ and $[R]_T = 36\ \mu M$ (*i.e.*, Set **V** of Table 2, with dotted line) or $[R]_T = 90\ \mu M$ (*i.e.*, set Set **IV**, with solid line). In Fig. 9(a) we show the results obtained for a source with $n_c = 10$ open IP_3Rs and an isolated "sensing" IP_3R ($n_s = 1$) at $d = 0.6\ \mu m$. In Figs. 9(b)-(c) we show the results obtained for a sensing cluster with $n_s = 5$ IP_3Rs located at a distance, $d = 1.4\ \mu m$, from the source which has $n_c = 10$ simultaneously open IP_3Rs in (b) and $n_c = 50$ in (c). The change in P_0 with increasing $[R]_T$ is unobservable at $d = 1.4\ \mu m$ for both $n_c = 10$ (≤ 0.004) and $n_c = 50$ while it can be ~ -0.045 at $d = 0.6\ \mu m$ when $[R]_T$ is varied from 36 to 90 μM. In particular, the difference of the open probability between these two simulations is $\Delta P_0(d = 0.6\mu m, t) \approx -0.034$ at $t = d/V$ with $V \sim 10\ \mu m/s$, a typical wave velocity.

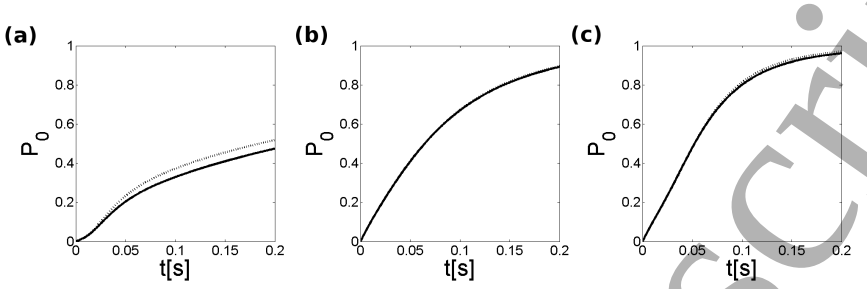

Figure 9: Probability, $P_0(d,t)$, that an IP_3R within a cluster with n_s IP_3Rs located at a distance, d, from a point source with n_c open channels becomes open by time t. (a) $d = 0.6\ \mu m$, $n_c = 10$ and $n_s = 1$. (b) $d = 1.4\ \mu m$, $n_c = 10$ and $n_s = 5$. (c) $d = 1.4\ \mu m$, $n_c = 50$ and $n_s = 5$. Experiments with $[F]_T = 36\ \mu M$, $[EGTA]_T = 45\ \mu M$ and $[R]_T = 36\ \mu M$ (*i.e.*, Set **V** of Table 2, with dotted line) or $[R]_T = 90\ \mu M$ (*i.e.*, set Set **IV**, with solid line).

4 Discussion and Conclusions

We have studied the role of buffers on IP_3R-mediated Ca^{2+} signals observing the signals simultaneously with two dyes of different kinetics. Previous works on the effects of Ca^{2+} buffers drew conclusions "indirectly" by observing the Ca^{2+}-bound dye distributions in the presence of varying concentrations of exogenous buffers [17, 18, 27]. Different modeling strategies and numerical simulations were then used to interpret the results [24, 25, 28, 29]. In the present paper we have made visible the invisible by observing the signals simultaneously with two dyes, Rhod-2 and Fluo-4, of different kinetics. In this way, we could study the role of slow and fast buffers on the emerging signal more directly from the observations. Most dyes are designed and/or chosen so that they perturb the signals the least and yet can report on fast Ca^{2+} changes. This implies that their kinetics is usually fast. In fact, Fluo-4 is only slightly faster than Rhod-2. In spite of this, the analysis of the changes induced when the concentration of one of these two dyes was varied allowed us to infer trends.

We first focused on how some properties that characterize the release of Ca^{2+} during localized signals (puffs) changed when varying the dyes and EGTA concentrations. As a first step, we produced a proof of concept by checking that the observed puff properties varied as expected for increasing concentrations of a slow or a fast buffer when increasing $[R]_T$ or $[F_T]$, respectively (see Supplementary Material). This allowed us to identify the variations produced by either one of the dyes with those produced by slow

or fast buffers. We subsequently investigated whether the observed changes were merely observational or could be attributed to modifications in the underlying Ca^{2+} release. To this end we used numerical simulations to identify quantities, A_{lib-F} and A_{lib-R}, that could compensate for the different amounts of Ca^{2+} that are trapped by one of the dyes when the concentration of the other is varied (Supplementary Material). These quantities require the knowledge of the Ca^{2+}-bound dye concentration to be computed. Our previous work on the analysis of Ca^{2+} images obtained with single wavelength dyes [26] prescribes how to estimate these concentrations. Using this tool, we computed, for our experiments, $[CaF]$ and $[CaR]$ and then used Eq. (11) to derive A_{lib-F} and A_{lib-R}. We further calculated the corresponding growth rates, $GR\text{-}A_{lib-F}$ and $GR\text{-}A_{lib-R}$, that reflect more directly the Ca^{2+} current that underlies the observed events (see Materials and Methods). Thus, in the first part of the analysis we characterized each release event by a few properties. We then looked at the spatial distribution of Ca^{2+}-bound to either dye during the observed events and analyzed how they changed with the dye concentrations. In order to interpret the experimental observations we performed numerical simulations. The numerical studies gave us the Ca^{2+}-bound dye spatio-temporal distributions that could be expected from a very localized site of release. They also allowed us to estimate the Ca^{2+}-mediated coupling between sites of release by computing the open probability of a channel located at a certain distance from the source (Eq. 10). We describe in what follows the main results obtained from these various analyses.

4.1 The changes observed with increasing $[R]_T$ highlight the effect of slow buffers on the disruption of inter-cluster CICR.

The cumulative distribution functions of the quantities that characterize the Ca^{2+}-release rate, A_{lib-F} and $GR\text{-}A_{lib-F}$, showed an increase of $\langle A_{lib-F} \rangle$ and of $\langle GR\text{-}A_{lib-F} \rangle$ with increasing $[R]_T$ (Figs. 4(a) and (b)). The Kolmogorov-Smirnov (KS) test applied to these data rejects the null hypothesis that the CDFs of $GR\text{-}A_{lib-F}$ compared in Fig. 4(b) come from the same continuous distribution with a 99% significance level ($p_{value} = 4.4 \cdot 10^{-4}$), but it does not reject it in the case of the CDFs of A_{lib-F} compared in Figs. 4(a) ($p_{value} = 0.19$). The test applied to the CDFs of A_{lib-F} obtained in the experiments with $[EGTA]_T = 90\ \mu M$, however, rejects the hypothesis that the data obtained in the absence of Rhod-2 (set **III**) come from the same distribution as those obtained with Rhod-2 (sets **II** or **I**) with a 99% significance level ($p_{value} = 2.1 \cdot 10^{-4}$ and $p_{value} = 4.6 \cdot 10^{-5}$, respectively, data not shown).

These results are consistent with an increase of the largest Ca^{2+} current that underlies the observed puffs as $[R]_T$ is increased. They are also compatible with the changes observed in the Ca^{2+} waves elicited with varying $[R]_T$ as illustrated in Fig. 4(c) where we have plotted the CDFs of the velocity of the waves observed in the Fluo-4 channel (V_F) in experiments of Set **IV** (dotted line) and Set **V** (solid line). Although the KS test cannot reject the hypothesis that both data sets come from the same distribution, the p_{value} is very small ($p_{value} = 0.15$) and the mean velocity gets bigger when $[R]_T$ is increased. These results support our interpretation of the observations reported in [21]. In that paper we hypothesized that the larger concentration of a slow buffer resulted in a more efficient disruption of the inter-cluster CICR and, therefore, in the existence of signals of larger underlying Ca^{2+} currents that remained as puffs without turning into waves. Under this assumption it is reasonable that the events that turn into waves be, on average, of larger velocity as $[R]_T$ is increased. Thus, the results of Figs. 4(a)-(c) can be explained consistently within this interpretation.

4.2 The changes observed with increasing $[F]_T$ highlight the dual role of fast buffers on IP_3R-mediated Ca^{2+}-release events.

The cumulative distribution functions of A_{lib-R} and of GR-A_{lib-R}, plotted in Figs. 4(d) and (e), showed a slight decrease of $\langle A_{lib-R}\rangle$ and of $\langle GR\text{-}A_{lib-R}\rangle$ with increasing $[F]_T$. The lack, in the experiments performed with no Fluo-4 (Set **VI**), of the events with the largest A_{lib-R} observed when Fluo-4 was present (Set **IV**) was also apparent in Fig. 4(d). The distribution of the A_{lib-R} growth rate (Fig. 4(e)) also shifted towards smaller values as $[F]_T$ increased. The KS test, however, does not reject the hypotheses that the CDFs of A_{lib-R} and of GR-A_{lib-R} compared in these figures come from the same distribution ($p_{value} = 0.42$ in (d) and 0.24 in (e)). Although mild, the observed changes are an indication that the Ca^{2+} current, not just the Ca^{2+}-bound Rhod-2 concentration, decreased when the concentration of the fast dye, Fluo-4, increased. This seems to contradict the idea that the presence of a fast buffer (Fluo-4) alleviates IP_3R-inhibition allowing more Ca^{2+} to be released. We must remember, however, that A_{lib-D} and GR-A_{lib-D} ($D = F$ for Fluo-4 and $D = R$ for Rhod-2) are reporters of the maximum Ca^{2+} concentration and of the Ca^{2+} current, not of the total Ca^{2+} released during the time course of the event. In order to estimate the latter we computed I_{lib-R} (see Materials and Methods). As shown in Fig. 4(f), the I_{lib-R} distribution remained more or less unchanged with varying Fluo-4.

The results on A_{lib-R}, $GR\text{-}A_{lib-R}$ and I_{lib-R} together with the larger values of the time, $t_{r,R}$, during which there is Ca^{2+} release as $[F]_T$ is increased (Fig. SM4(b)) support the hypothesis that fast buffers may play different roles during IP_3R-mediated Ca^{2+} signals. Depending on their concentration and on the IP_3R spatial organization they can either moderate CICR within the cluster leading to signals with smaller Ca^{2+} currents or they can buffer enough Ca^{2+} so as to prevent IP_3R-inhibition allowing the almost immediate re-opening of IP_3Rs and a longer cycle of Ca^{2+} release. The combination of a longer release at a slower rate can eventually lead to an almost invariant total released $[Ca^{2+}]$ with varying buffer (in this case, Fluo-4) concentration as observed in our experiments.

4.3 Differences in the spatial distribution of Ca^{2+} bound to Rhod-2 and Fluo-4 indicate that Ca^{2+} is released from relatively wide regions.

We then compared the spatio-temporal distributions of $[CaR]$ and $[CaF]$ for the various experiments. To this end we derived estimates of these concentrations from the observed fluorescence distributions as explained in Sec. 2.3.3. The analysis of the distance, δ, between the locations of the maxima of $[CaR]$ and $[CaF]$ for the Ca^{2+} puffs that we could observe simultaneously with both dyes showed distributions that were concentrated around small δ values for the experiments with $[R]_T = 90\ \mu M$ (about 85% of the observations had $\delta \leq 0.2\ \mu m$ (see Fig. 5(b) and (d)) and that embraced a larger range (up to $\sim 1\ \mu m$) for those with $[R]_T = 36\ \mu M$ (Fig. 5(a) and (c)). As illustrated in the simulations of Fig. 8, if all the release came from a single point, the maxima of $[CaR]$ and $[CaF]$ should occur at that point. The large δ values observed in Figs. 5 (a) and (c) are an indication that Ca^{2+} can be released from a relatively wide spatial region during puffs and reflect the differential ability of both dyes to trap Ca^{2+}. Fig. 6 further illustrated these aspects. There we observed that for $[R]_T = 36\ \mu M$ (Figs. 6(a) and (c)), the points where $[CaR]$ was above 60% of its corresponding maximum value over the whole image, CaR_{max}, hardly ever coincided with those where $[CaF] > 0.6CaF_{max}$. In this case Rhod-2 was most likely trapping Ca^{2+} in regions where Fluo-4 was locally depleted. For $[R]_T = 90\ \mu M$ (Figs. 6(b) and (d)) there was more co-localization as reflected by the larger overlapping areas. Here Rhod-2 was almost as efficient as Fluo-4 in trapping Ca^{2+} where the release occured at the fastest pace. In either case, this competition was different depending on $[EGTA]_T$. For low $[EGTA]_T$ (Fig. 6(b)), $[CaR]$ was relatively large over a wider spatial and temporal region than $[CaF]$. For

$[EGTA]_T$=90 μM (Fig. 6(d)) the space and time extent of CaR and CaF were similar. It seems as if in Fig. 6(d) it was EGTA (as it was Rhod-2 in Figs. 6(a) and (c)) the slow buffer that could only trap Ca^{2+} away from the regions of fastest release. This was further supported by the fact that the maximum variation in $[CaR]$ was almost 40% larger in Fig. 6(d) than in Figs. 6(b) and (c) and 60% larger than in Fig. 6(a), while the maximum variation in $[CaF]$ remained almost unchanged in all four subfigures. The results of Figs. 5 and 6 indicate that the slow buffers that restrict the spatial extent of the distribution of Ca^{2+}-bound to faster buffers do it by trapping Ca^{2+} that is released at different spatial points from those that are clearly identified when looking at the distribution of Ca^{2+}-bound to fast dyes. This assumption is consistent with the results of the numerical simulations. As illustrated in Fig. 8 there are no differences in the numerically simulated versions of Figs. 6(a)-(d) as the concentrations of Rhod-2 or EGTA are varied if Ca^{2+} is released from a single point and the Ca^{2+} current is not changed. No changes were observed either in simulations with other values of the (localized) Ca^{2+} current (data not shown).

In order to further study the differences in the spatio-temporal distributions of $[CaR]$ and $[CaF]$ we analyzed examples of experimental observations in which apparently Ca^{2+} was released from various separate sites (Fig. 7). The examples showed that where Rhod-2 was capturing Ca^{2+} more efficiently (site 2 of Fig. 7(a)) the rise in $[CaF]$ was slowed down. Although Rhod-2 did not prevent the propagation of the signal between sites in this particular case it illustrated how it could do it in cases with less Ca^{2+} release (at sites 1 or 3). This same behavior was also observed in the wave illustrated in Figs. 7(c)-(d). In this figure we also looked at the region over which the Ca^{2+}-bound dye distributions were above 60% of their maximum values. We observed that this occurred over spatially contiguous regions that spanned up to 2.5 μm. Similar regions were obtained if the threshold was defined as 75% of the maximum fluorescence in each channel. The results of Figs. 5– 7 seem to indicate that Ca^{2+} release can occur over continuous regions that can be wider than what is supposed to be the typical inter-cluster separation ($\sim$ 1.4-2 μm). We then hypothesize that even though active IP_3Rs are largely clustered in sites 1.5-2 μm apart from one another, there could also be active IP_3Rs distributed in between.

4.4 Numerical simulations to interpret the experimental observations suggest the presence of "loose" functional IP_3Rs in between clusters.

In order to look into the possibility of having active IP_3Rs between clusters with more detail we performed numerical simulations of a model of the Ca^{2+} dynamics that included the presence of the two dyes and the exogenous buffer (EGTA) used in the experiments, an immobile endogenous buffer, Ca^{2+} pumps and a point source with n_c open channels at $t = 0$ that closed stochastically with mean time, $t_{open} = 20\ ms$. In particular we studied the probability, $P_0(d, t)$, that an IP_3R within a cluster with n_s "sensing" (IP_3-bound) IP_3Rs located at a distance, d, from the source became open by time, t. As shown in Fig. 9, the change of P_0 with varying $[R]_T$ was unobservable at $d = 1.4\ \mu m$ for both $n_c = 10$ and $n_c = 50$ while it could be ~ -0.045 at $d = 0.6\ \mu m$ when increasing $[R]_T$ from 36 to 90 μM even if there was only one sensing IP_3R in the latter while there were 5 in the simulations at $d = 1.4\ \mu m$. Furthermore, the variation in $P_0(d, t)$ between the cases with $[R]_T = 36\ \mu M$ and with $[R]_T = 90\ \mu M$ was ~ -0.034 at $d = 0.6\ \mu m$ for the simulation with $n_c = 10$ and $n_s = 1$ at a time, t, of the order of the time that it would take for a typical Ca^{2+} wave to travel a distance, $d = 0.6\ \mu m$. This difference, ~ -0.034, implies a reduction of the order of 14% in the open probability with respect to the value obtained for $[R]_T = 36\ \mu M$. Similar simulations performed for the conditions of the experiments with $[EGTA]_T = 90\ \mu M$ gave a 22% change in the open probability between the cases with $[R]_T = 0\ \mu M$ and $[R]_T = 90\ \mu M$ at $d = 0.6\ \mu m$, $t = 60\ ms$ with $n_s = 1$ sensing IP_3R and of 0.6% at $d = 1.4\ \mu m$, $t = 140\ ms$ with $n_s = 5$ sensing IP_3Rs. We also repeated the simulations in the presence of only one dye, Fluo-4, with $[EGTA]_T = 0\ \mu M$ and with $[EGTA]_T = 300\ \mu M$ to mimic some of the conditions of [17] that showed, respectively, global and localized only Ca^{2+} signals upon the same release of IP_3. The relative change of P_0 obtained with respect to the situation with no EGTA was less than 1% at $d = 1.4\ \mu m$, $t = 140\ ms$, with $n_s = 5$ sensing channels while it was $\sim 14\%$ at $d = 0.6\ \mu m$, $t = 60\ ms$ with $n_s = 1$ IP_3R (data not shown). These simulations indicate that the changes observed in the signals with increasing concentrations of slow buffers cannot be understood under the assumption that Ca^{2+} is released solely from IP_3R-clusters that are $\sim 1.4\ \mu m$ apart from one another. In combination with our experiments they further show that the presence of at least one functional IP_3R in between clusters may explain how slow buffers disrupt the Ca^{2+}-mediated coupling between IP_3R-clusters.

The presence of (diffusing) IP_3Rs outside clusters has been observed for

quite some time [37]. Single-particle tracking experiments revealed the co-existence of motile and immotile IP_3Rs with most of the latter organized in clusters [38]. Given that Ca^{2+} puffs have been observed to arise from fixed locations [39], the results of [38] suggested the identification between functional and immobile IP_3Rs. Our observations and analyses suggest that there are "loose" IP_3Rs between clusters that are functional (and probably immobile) and that they are key for the CICR coupling between IP_3R clusters.

Author Contributions

EP and LFL performed the experiments. EP performed the simulations. EP, LFL and SPD analyzed the experiments and simulations and wrote the paper. SPD conceived the work.

Acknowledgments

This research has been supported by Universidad de Buenos Aires (UBACyT 20020130100480BA) and Agencia Nacional de Promoción Científica y Tecnológica (PICT 2013-1301 and PICT 2015-3824). SPD is a member of Carrera del Investigador Científico (Consejo Nacional de Investigaciones Científicas y Técnicas).

References

[1] Berridge, M., M. Bootman, and P. Lipp, 1998. Calcium - a life and death signal. *Nature* 395:645–648.

[2] Bootman, M. D., T. J. Collins, C. M. Peppiatt, L. S. Prothero, L. MacKenzie, P. D. Smet, M. Travers, S. C. Tovey, J. T. Seo, M. J. Berridge, F. Ciccolini, and P. Lipp, 2001. Calcium signalling an overview. *Seminars in Cell & Developmental Biology* 12:3 – 10.

[3] Choe, C.-u., and B. E. Ehrlich, 2006. The Inositol 1,4,5-Trisphosphate Receptor (IP3R) and Its Regulators: Sometimes Good and Sometimes Bad Teamwork. *Science Signaling* 2006:re15–re15.

[4] Foskett, J. K., C. White, K.-h. Cheung, and D.-o. D. Mak, 2007. Inositol Trisphosphate Receptor Ca2+ Release Channels. *Physiological Reviews* 87:593–658.

[5] Fabiato, A., 1983. Calcium-induced release of calcium from the cardiac sarcoplasmic reticulum. *Am J Physiol* 245:1–15.

[6] Sun, X.-P., s. N. Callamara, J. S. Marchant, and I. Parker, 1998. A continuum of InsP3-mediated elementary Ca2+ signalling events in Xenopus oocyte. *The Journal of Physiology* 509:67–80.

[7] Smith, I. F., and I. Parker, 2009. Imaging the quantal substructure of single IP3R channel activity during Ca2+ puffs in intact mammalian cells. *Proceedings of the National Academy of Sciences* 106:6404–6409.

[8] Solovey, G., and S. P. Dawson, 2010. Intra-Cluster Percolation of Calcium Signals. *PLoS ONE* 5:e8997.

[9] Yao, Y., J. Choi, and I. Parker, 1995. Quantal puffs of intracellular Ca2+ evoked by inositol trisphosphate in Xenopus oocytes. *The Journal of physiology* 482 (Pt 3:533–553.

[10] Dolmetsch, R. E., R. S. Lewis, C. C. Goodnow, and J. I. Healy, 1997. Differential activation of transcription factors induced by Ca2+ response amplitude and duration. *Nature* 386:855–858.

[11] De Koninck, P., and H. Schulman, 1998. Sensitivity of CaM Kinase II to the Frequency of Ca2+ Oscillations. *Science* 279:227–230.

[12] Lüscher, C., and R. Malenka, 2012. NMDA Receptor-Dependent Long-Term Potentiation and Long-Term Depression (LTP/LTD). *Cold Spring Harbor Perspectives in Biology* 4:a005710.

[13] Nelson, M. T., H. Cheng, M. Rubart, L. F. Santana, A. D. Bonev, H. J. Knot, and W. J. Lederer, 1995. Relaxation of Arterial Smooth Muscle by Calcium Sparks. *Science* 270:633–637.

[14] Nishiyama, M., K. Hong, K. Mikoshiba, M.-m. Poo, and K. Kato, 2000. Calcium stores regulate the polarity and input specificity of synaptic modification. *Nature* 408:584–588.

[15] Falcke, M., 2004. Reading the patterns in living cells-the physics of ca2+ signaling. *Advances in Physics* 53:255–440.

[16] Kudla, J., O. Batistic, and K. Hashimoto, 2010. Calcium Signals: The Lead Currency of Plant Information Processing. The Plant Cell. *The Plant Cell* 22:541–563.

[17] Dargan, S. L., and I. Parker, 2003. Buffer kinetics shape the spatiotemporal patterns of IP3-evoked Ca2+ signals. *The Journal of physiology* 553:775–788.

[18] Dargan, S. L., B. Schwaller, and I. Parker, 2004. Spatiotemporal patterning of IP3-mediated Ca2+ signals in Xenopus oocytes by Ca2+-binding proteins. *The Journal of physiology* 556:447–461.

[19] Paredes, R. M., J. C. Etzler, L. T. Watts, W. Zheng, and J. D. Lechleiter, 2008. Chemical calcium indicators. *Methods (San Diego, Calif.)* 46:143–51.

[20] Marchant, J. S., and I. Parker, 2001. Role of elementary Ca 2+ puffs in generating repetitive Ca 2+ oscillations. *EMBO Journal* 20:65–76.

[21] Piegari, E., L. Sigaut, and S. Ponce Dawson, 2015. Ca2+ images obtained in different experimental conditions shed light on the spatial distribution of IP3 receptors that underlie Ca2+ puffs. *Cell Calcium* 57:109–119.

[22] Ventura, A. C., L. Bruno, A. Demuro, I. Parker, and S. P. Dawson, 2005. A model-independent algorithm to derive Ca2+ fluxes underlying local cytosolic Ca2+ transients. *Biophysical journal* 88:2403–2421.

[23] Bruno, L., G. Solovey, A. C. Ventura, S. Dargan, and S. P. Dawson, 2010. Quantifying calcium fluxes underlying calcium puffs in Xenopus laevis oocytes. *Cell Calcium* 47:273–286.

[24] Shuai, J., J. E. Pearson, and I. Parker, 2008. Modeling Ca2+ Feedback on a Single Inositol 1,4,5-Trisphosphate Receptor and Its Modulation by Ca2+ Buffers. *Biophysical Journal* 95:3738 – 3752.

[25] Rudiger, S., C. Nagaiah, G. Warnecke, and J. Shuai, 2010. Calcium Domains around Single and Clustered {IP3} Receptors and Their Modulation by Buffers. *Biophysical Journal* 99:3 – 12.

[26] Piegari, E., L. Lopez, E. Perez Ipiña, and S. Ponce Dawson, 2014. Fluorescence fluctuations and equivalence classes of Ca2+ imaging experiments. *PLoS ONE* 9.

[27] Callamaras, N., and I. Parker, 2000. Phasic characteristic of elementary Ca2+ release sites underlies quantal responses to IP3. *The EMBO Journal* 19:3608–3617.

[28] Fraiman, D., and S. P. Dawson, 2014. Buffer regulation of calcium puff sequences. *Physical Biology* 11:016007.

[29] Rüdiger, S., J. W. Shuai, and I. M. Sokolov, 2010. Law of Mass Action, Detailed Balance, and the Modeling of Calcium Puffs. *Phys. Rev. Lett.* 105:048103.

[30] Diambra, L., and J. S. Marchant, 2011. Inositol (1,4,5)-trisphosphate receptor microarchitecture shapes Ca 2+ puff kinetics. *Biophysical Journal* 100:822–831.

[31] Solovey, G., and S. P. Dawson, 2010. Intra-cluster percolation of calcium signals. *PLoS ONE* 5:1–8.

[32] Solovey, G., D. Fraiman, and S. P. Dawson, 2011. Mean field strategies induce unrealistic non-linearities in calcium puffs. *Frontiers in Physiology* 2 AUG:1–11.

[33] Sigaut, L., M. Barella, R. Espada, M. L. Ponce, and S. P. Dawson, 2011. Custom-made modification of a commercial confocal microscope to photolyze caged compounds using the conventional illumination module and its application to the observation of Inositol 1,4,5-trisphosphate-mediated calcium signals. *Journal of biomedical optics* 16:066013.

[34] MATLAB, 2010. version 7.10.0 (R2010a). The MathWorks Inc., Natick, Massachusetts.

[35] Zimmermann, T., 2005. Spectral imaging and linear unmixing in light microscopy. *Microscopy techniques* 1308–1310.

[36] De Young, G. W., and J. Keizer, 1992. A single-pool inositol 1,4,5-trisphosphate-receptor-based model for agonist-stimulated oscillations in Ca2+ concentration. *Proceedings of the National Academy of Sciences* 89:9895–9899.

[37] Ferreri-Jacobia, M., D.-O. D. Mak, and J. K. Foskett, 2005. Translational Mobility of the Type 3 Inositol 1,4,5-Trisphosphate Receptor Ca2+ Release Channel in Endoplasmic Reticulum Membrane. *Journal of Biological Chemistry* 280:3824–3831.

[38] Dickinson, G. D., K. L. Ellefsen, S. P. Dawson, J. E. Pearson, and I. Parker, 2016. Hindered cytoplasmic diffusion of inositol trisphosphate restricts its cellular range of action. *Science Signaling* 9:ra108–ra108.

[39] Smith, I. F., S. M. Wiltgen, J. Shuai, and I. Parker, 2009. Ca2+ Puffs Originate from Preestablished Stable Clusters of Inositol Trisphosphate Receptors. *Science Signaling* 2:ra77–ra77.